

## Chapter 2

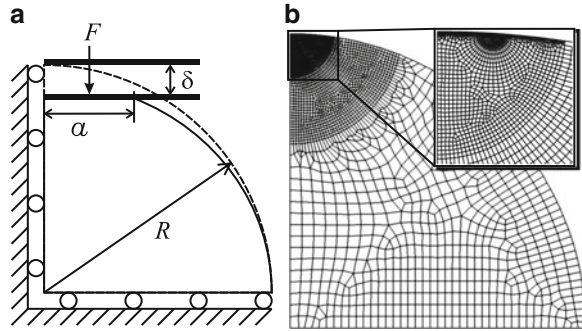
# Asperity Creep Under Constant Displacement

As pointed out in Chap. 1.1, the behavior of an elastic-perfectly plastic hemisphere in contact with a rigid plane has received a great deal of interest. Many recent efforts used the method of Finite Element modeling, from which empirical laws of the behavior were extracted. In this chapter, an analysis of the transient creep behavior of an asperity is presented. The aim is to gain a fundamental understanding of the root cause of transient effects in friction by investigating the creep behavior of the individual junction. This study restricts itself to the stress relaxation process of an asperity at a fixed interference. For an analysis of the behavior of an asperity under the—more complicated—constant force boundary condition, see Chap. 3. It is further assumed that the asperity is in the fully plastic contact regime. The term *fully plastic* is used here in accordance with Kogut and Etsion[82, 128], meaning that everywhere along the contact line the material has reached the yield stress.

Earlier studies on the influence of creep on the contact of a sphere and a flat focused on the complementary problem of a rigid sphere indenting an elasto-plastic flat [41, 172, 179, 187, 207]. The specific aim of these studies was often to derive or test a constitutive material creep law from a measured indenter response. In recent years, new applications for nano-indentation of polymers or biological tissue have invigorated the field. The problem was studied both empirically, e.g. by Mulhearn and Tabor [172], as well as analytically, e.g. by Bower et al. [41] or by Finite Element simulations, e.g. by Ogbonna et al.[179]. However, because the problem studied by these authors is complementary to the one studied here, it shows a fundamentally different behavior. During the revision of [100], the author became aware of the recent publication [49] by Brot et al., who independently have presented an FEA study on creep in asperities. While their approach is very similar to the one presented here, their study focused on a different set of boundary conditions, assuming constant force instead of constant displacement of the contacting flat. Also, Brot et al. [49] have used a power law instead of an exponential material creep law.

The organization of this chapter is as follows: in Sect. 2.1, the setup of the Finite Element simulation is described, including the material laws used for modeling the creep behavior. Section 2.2 discusses the simulation results. Section 2.2.1 focuses

**Fig. 2.1** (a) Sketch of the geometry. (b) The Finite Element mesh used for the simulation



on a comparison of the relevant aspects of asperity evolution known from previous research to the present simulation. In the following Sect. 2.2.2, an overview of the new simulation results of the creep behavior of an asperity is given. In Sects. 2.2.3 and 2.2.4, more details related to the area and stress evolution are presented, giving empirical laws for the behavior. A short discussion of the results of this chapter can be found in Sect. 2.3.

## 2.1 Modeling and Simulation

The basic geometry under analysis is depicted in Fig. 2.1a: a half-sphere with an undeformed radius  $R$  is in contact with a rigid flat. Because of the symmetry, it is sufficient to model a quarter sphere in 2D, using an axial symmetric element formulation. The natural boundary condition at the symmetry line is a sliding (roller) contact, i.e. a constraint in the radial direction. At the base of the sphere, sliding contact is assumed as well, i.e. constraint in the vertical direction. This boundary condition was chosen in order to make the results comparable to studies published by Kucharski et al. [149] and Kogut and Etsion [144]. An equally realistic boundary condition would be full constraint, as used, for example, by Jackson and Green [126, 128]. However, it was checked that the results were independent of the exact boundary conditions at the sphere base using several typical simulation runs. Even for sliding contact, the deformations at the sphere base were negligible. Invoking Saint-Venant's principle, this fact is easily understood in that the base is far away from the contact zone at the sphere's top and much more massive than the deformed sphere top, yielding negligible deformation for an equivalent system of forces.

The simulations were performed using the commercial Finite Element simulation code ANSYS 11, with a mesh of about 3,300 predominantly rectangular elements with quadratic shape functions. Meshing was conducted based on a series of regions, with finer meshes in proximity to the contact area and a coarser mesh for the region near the base of the sphere. In addition, the boundary of the sphere in the contact

**Table 2.1** Overview of parameter ranges used for simulation runs

No.	Varied parameter	Range
1	None ( <i>reference</i> )	$R = 1 \text{ mm}$ , $E = 200 \text{ GPa}$ , $\nu = 0.33$ , $\sigma_Y = 400 \text{ MPa}$ , ( $C_1 = 1 \cdot 10^{-4} \text{ s}^{-1}$ ), $C_2 = 10/\sigma_Y$ , $\delta = 100\delta_c$
2	Radius $R$	0.1–10 mm
3	Interference $\delta$	$25\delta_c$ – $600\delta_c$
4	Poisson's ratio $\nu$	0.28–0.38
5	Yield stress $\sigma_Y$	200–2,000 MPa
6	Young's modulus $E$	70–300 GPa
7	MCL parameters	$C_1 = 10^{-3} \text{ to } 10^{-5} \text{ s}^{-1}$ , $C_2 = 5/\sigma_Y$ – $15/\sigma_Y$

region was meshed more finely than the bulk to facilitate accurate detection of the contact radius (see Fig. 2.1b for a graphical representation of the mesh). The following mesh parameters were typically used: a semicircular region with a radius of  $0.15R$  centered on the uppermost tip of the sphere was meshed with a default mesh size of approximately  $0.005R$ . In a semicircular region centered on the outer rim of the contact zone with a radius of  $0.02R$ , the default mesh size was reduced to  $0.002R$ . At the boundary, a local mesh refinement with at least 200 mesh nodes at the edge of the contact region and 50 nodes otherwise was imposed. These finely meshed regions consisted of about 1,500 or 45 % of the elements. In a wider region of semicircular shape with a radius of  $0.38R$  around the sphere tip, the mesh size was increased to  $0.01R$  with no refinement near the boundary, resulting in 1,050 or about 35 % of the elements. This meshing region was sized to comprise the high-stress regions of the model (see Fig. 2.4, for the reference parameter set 1 in Table 2.1 on page 19). The rest of the model was meshed with a mesh size of  $0.04R$  and included about 700 or 20 % of the elements.

The contact was implemented using a rigid line target element to model the rigid flat. The choice of a purely Lagrangian contact algorithm yielded high numerical accuracy while retaining generally good convergence. Chatter, or bouncing, was not a problem for the system under consideration. The contact radius,  $a$ , (see Fig. 2.1a), contact force  $F$ , and interference  $\delta$ , were measured every time a node established, or lost, contact with the rigid flat. Therefore, a fine mesh in the contact zone was not only necessary for an accurate calculation of plastic strain, but also for a precise determination of the contact area.

A geometrically nonlinear formulation was used (NLGEOM), which corresponds to a Lagrangian strain formulation. However, as was checked for several typical parameter choices, a small strain formulation would have been sufficient for almost all parameter choices and will therefore be used for the analytical results reported in this chapter. The material of the sphere was assumed to be isotropic and elastic-perfectly plastic; no hardening rule was used. The plasticity behavior was based on the (isotropic) von Mises yielding criterion, with an associative flow rule.

According to standard small strain continuum theory, the total strain tensor  $\boldsymbol{\varepsilon}_{tot}$  can be separated into the creep, plastic and elastic strain tensors according to

$$\dot{\boldsymbol{\varepsilon}}_{tot} = \dot{\boldsymbol{\varepsilon}}_{cr} + \dot{\boldsymbol{\varepsilon}}_{pl} + \dot{\boldsymbol{\varepsilon}}_{el}. \quad (2.1)$$

In the creep process, the elastic strain  $\boldsymbol{\varepsilon}_{el}$  decreases in favor of the creep strain  $\boldsymbol{\varepsilon}_{cr}$ , thus reducing the total stress

$$\boldsymbol{\sigma} = \mathbf{C} : \boldsymbol{\varepsilon}_{el} \quad (2.2)$$

with  $\mathbf{C}$  the elasticity tensor (In this notation, the double colon  $:$  marks a reduction of the full tensor grade by two, i.e. a multiplication of a tensor of the 4th grade with a tensor of the 2nd grade yields a tensor of 2nd grade). It is sufficient to formulate the uniaxial creep law  $\dot{\varepsilon}_{cr}(\sigma)$ , where  $\varepsilon_{cr}$  and  $\sigma$  denote the equivalent strain and stress (von Mises stress), respectively. The full creep rate tensor,  $\dot{\boldsymbol{\varepsilon}}_{cr}$ , is then derived by choosing the creep strain updates normal to the yield surface. For the von Mises yield surface

$$F(\boldsymbol{\sigma}) = \sigma = \sqrt{3J_2} = \sigma_Y, \quad (2.3)$$

where  $\sigma_Y$  is the yield stress and  $J_2 = \frac{1}{2}\mathbf{s} : \mathbf{s}$  is the second invariant of the stress deviator tensor  $\mathbf{s} = \boldsymbol{\sigma} - \frac{1}{3}\text{tr}(\boldsymbol{\sigma})\mathbf{I}$ , the full creep tensor is then

$$\dot{\boldsymbol{\varepsilon}}_{cr} = \frac{\dot{\varepsilon}_{cr}}{f_{cr}} \frac{\partial F(\boldsymbol{\sigma})}{\partial \boldsymbol{\sigma}}. \quad (2.4)$$

The factor  $f_{cr}$  is such that  $\boldsymbol{\sigma}$  and  $\boldsymbol{\varepsilon}_{cr}$  are work conjugate, i.e.  $f_{cr} = \frac{1}{\sigma} \boldsymbol{\sigma} : \frac{\partial F(\boldsymbol{\sigma})}{\partial \boldsymbol{\sigma}}$ .

The choice of the uniaxial creep law therefore determines the physics of the problem. A power law

$$\dot{\varepsilon}_{cr} = B\sigma^n \quad (2.5)$$

with an exponent  $n$  between 1 and 8 seems to be the prevalent model for high-stress dislocation creep. However, recent publications in the field of friction mostly rely on exponential creep models

$$\dot{\varepsilon}_{cr} = B' \exp(\beta\sigma). \quad (2.6)$$

For example, the formulation by Brechet [43], deriving the Rice–Ruina friction law from creep arguments, used an exponential creep law. Persson [191] presented basically the same derivation, augmented by his own theory of creep [192] which also proposes an exponential creep law. In some publications [93], it is stated that the power creep law is only applicable to low stresses while exponential creep is the valid creep law for high stresses. Moreover, the exponential and power creep law can sometimes be hard to distinguish experimentally. From a simulation point of view, the assumption of an exponential creep yields nonzero creep  $\dot{\varepsilon}_{cr}$  for disappearing

stress  $\sigma$ , which can sometimes lead to convergence issues. Therefore, the Garofalo [93] or hyperbolic sine power creep law

$$\dot{\epsilon}_{cr} = C_1 \sinh(C_2 \sigma)^n \quad (2.7)$$

was adopted in the present work, which, for small stresses  $\sigma$ , reduces to a power law of the form of Eq. (2.5) with  $C_1 \alpha^n = B$ , and for high stresses to an exponential law (2.6) with  $C_1 = B'2^n$  and  $C_2 n = \beta$ . It should be noted that Persson, in his creep theory [192], presented exponential creep as the high-stress limit case of his theory (inversion of formula (37) in [192]) while a linear relation  $\dot{\epsilon}_{cr} = \eta \sigma$  [192, formula (38)] is presented as the low-stress limit. For  $n = 1$ , this relation is reproduced accurately by the Garofalo type creep which can therefore be seen as a good quasistatic approximation to Persson's creep law. The further discussion will therefore be restricted to the case of  $n = 1$ . It should be noted that this is a minor limitation as far as high-stress creep is concerned, because a change in the exponent  $n$  has the same effect as a change in the creep parameter  $\tilde{C}_2 = nC_2$ .

The exponential nature of the creep law and the simple Euler creep integration used by ANSYS required a careful control of the integration time steps. As the creep constant  $C_1$  defines the characteristic time scale  $\tau \propto 1/C_1$  of the creep process, all results are presented using a scaled time. (See Eq. (2.33).) In the simulations,  $C_1$  was therefore chosen to optimize numerical convergence. In reality,  $C_1$  usually shows an exponential dependence on the temperature  $T$ , i.e.

$$C_1 = \tilde{C}_1 \exp(-Q_{cr}/kT) \quad (2.8)$$

where  $Q_{cr}$  is the activation energy for creep. Moreover,  $C_1$  varies widely even for small changes of material composition, let alone for material classes. At 400 K and for metals, values between  $10^{-6}$  and  $1 \text{ s}^{-1}$  are not out of question, and reliable values are hard to achieve experimentally. In the further discussion, as an example, an iron-like material will be considered with an exemplary value of  $C_1 = 10^{-3} \text{ s}^{-1}$  (see for example Frost and Ashby [89]).

The wide range of typical values for  $C_1$  raises the question if the creep process of an asperity is actually fast enough to explain effects like the time- and velocity-dependence of friction. For polymers, the creep activation energy  $Q_{cr}$  correlates with the glass transition temperature as  $T_G/k$ , which is much lower than, for example, the melting temperature of a metal. Therefore, it is immediately obvious that for these kinds of materials, an effect is measurable, as proven by the experiments by Dieterich and Kilgore [72], and relevant to friction processes [49]. For metals, macroscopic creep processes at room temperature usually occur in the order of days rather than seconds. One might therefore be tempted to rule out effects due to creep for these kinds of materials. However, it should be stressed that, especially in multi-scale contact models [130], highly loaded microscopic asperities deep in the plastic loading regime occur. These naturally do creep considerably faster than a macroscopic system, which is moreover usually designed to operate far from its yielding limit. The same argument holds to a lesser degree also for statistical contact

models, as shown by the calculation by Brechet and Estrin [43] who predicted a measurable effect for sliding velocities in the order of  $v = 10^{-4} - 10^{-3}$  cm/s. Adding to this effect, the flash temperature at the junction interfaces under sliding friction can be decidedly higher than that of the surrounding material, easily reaching as high as half the melting temperature [38]. Because of the exponential dependency of  $C_1$  on the temperature  $T$ , this effect can probably not be neglected. In the discussion in Sect. 2.3, the simulation results will be interpreted in the light of this question.

The integration time steps taken in the simulation were manually controlled, with an exponential distribution of the time steps  $t_i = t_{\min} \exp(\ln(t_{\max}/t_{\min}) \frac{i}{N})$ . Here,  $t_{\min}$  and  $t_{\max}$  denote the lower and upper limits of the simulation time frame and  $N$  is the number of time steps, usually chosen as  $N = 400$ , depending on the parameter choice. The sufficiency of this number was tested by increasing the number of time steps by 50 % and ensuring that the resulting force and area evolution curves changed only within the limits of their numerical scatter, which is about 2 %. A typical simulation run with the default mesh and number of time steps took between 1 and 2 h on a 1.6 GHz Itanium2 computing node with 4 GB of RAM.

## 2.2 Simulation Results of Stress Relaxation

### 2.2.1 Static Deformation

A series of simulation experiments were conducted to measure the stress relaxation of a half sphere with a constant interference boundary condition. This type of simulation consisted of two steps: (a) the approach of the rigid contact plane to a predefined interference  $\delta$ , (b) creep relaxation at fixed interference  $\delta$ . In stage (a), the stress buildup stage, creep effects were neglected. Physically, this is equivalent to a fast approach where creep has a negligible influence. The behavior of an asperity in this stage is well understood, and can therefore be used to validate the simulation system. In this section, the relevant equations are summarized and the results of this simulation study are compared to previously published results. In total, the results of the present chapter have been derived from several hundred simulation experiments, many of which were statistically averaged to achieve the required low error tolerances.

Following Jackson and Green [128], the contact area  $A$  in dependence on the interference  $\delta$  during elasto-plastic and fully plastic compression follows to a good approximation the power law

$$A = A_c \frac{\delta}{\delta_c} \left( \frac{\delta}{1.9\delta_c} \right)^{0.14 \exp(23\sigma_Y/E)} \quad \text{for } \delta \geq 1.9\delta_c, \quad (2.9)$$

where

$$\delta_c = \left( \frac{\pi C \sigma_Y}{2E'} \right)^2 R \quad \text{with} \quad C = 1.295 \exp(0.736\nu) \quad (2.10)$$

marks the onset of plastic yield [131]. The Hertz modulus  $E'$  is defined by

$$E' = E/(1 - \nu^2) \quad (2.11)$$

for the contact between a sphere and a rigid flat.<sup>1</sup> The critical area

$$A_c = \pi R \delta_c \quad (2.12)$$

is the contact area at the onset of plastic yield which can be calculated according to Hertz's contact theory. Furthermore,  $\nu$  and  $E$  denote the Poisson ratio and the Young modulus of the asperity. Slightly different empirical laws were formulated in [55, 82, 144] or [152] which lead to very similar results. The area due to Eq. (2.9) fits the present results in the range of the analyzed interferences  $25 - 400 \delta_c$  with a maximum error of about 5 %.

The hardness  $H$  of the material is (in the present work) defined as the average contact pressure in fully plastic contact. It is generally cited to be on the order of  $H \approx 2.8\sigma_Y$  [229]. In a recent study by Jackson and Green [128], the parameter dependence of the hardness for an elasto-plastic spherical asperity was studied in detail. Jackson and Green [128] fitted a Weibull function to a set of FEA simulations and found the following law for the hardness:

$$H_G = 2.84\sigma_Y \left[ 1 - \exp \left\{ -0.82 \left( \frac{a}{R} \right)^{-0.7} \right\} \right], \quad (2.13)$$

where  $a$  denotes the contact radius  $a = \sqrt{A/\pi}$ . This hardness was used by Jackson and Green to derive a generalized law for the contact force

$$F = F_c \left[ \exp \left\{ -\frac{1}{4} \left( \frac{\delta}{\delta_c} \right)^{5/12} \right\} \left( \frac{\delta}{\delta_c} \right)^{3/2} + \frac{4H_G}{C\sigma_Y} \left( 1 - \exp \left\{ -\frac{1}{25} \left( \frac{\delta}{\delta_c} \right)^{5/9} \right\} \right) \left( \frac{\delta}{\delta_c} \right) \right] \quad (2.14)$$

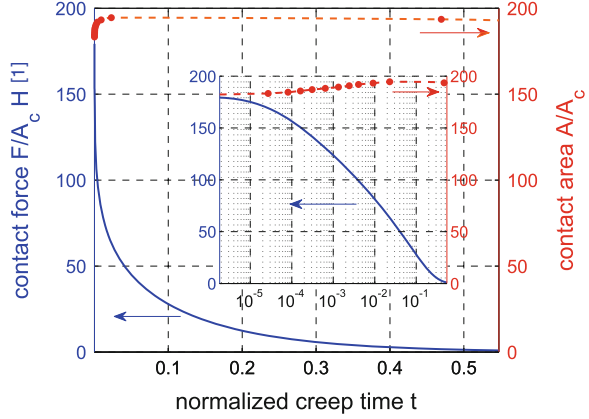
with  $F_c$  the critical force at the onset of yield

$$F_c = \frac{4}{3} \left( \frac{R}{E'} \right)^2 \left( \frac{1}{2} C \pi \sigma_Y \right)^3. \quad (2.15)$$

---

<sup>1</sup>For the general case of the contact between two spheres with Young moduli  $E_1$  and  $E_2$  and Poisson ratios of  $\nu_1$  and  $\nu_2$ , the Hertz modulus is  $E' = ((1 - \nu_1^2)/E_1 + (1 - \nu_2^2)/E_2)^{-1}$ .

**Fig. 2.2** Time evolution of force (*solid line*, left vertical axis) and contact area (*dashed line*, right vertical axis), inset shows the data in logarithmic scaling



In the reference simulation shown in Fig. 2.2 (for parameter set 1 in Table 2.1 on page 19), the initial force of  $F_0 = 180.9A_c H$  agrees within 2% with formula (2.14). Overall, the force levels in all simulations were found to agree with Jackson and Green's formulae within a 4% error level. The hardness values determined from the simulations showed a systematic error of about 3% compared to Jackson and Green's results, while the trends were reproduced very faithfully. Wherever hardness  $H$  is used, for example for normalization of the pressure  $p$ , the value from the simulation was used, and always the version immediately after loading (i.e. no creep has yet occurred).

Overall, the simulations were tested successfully against the established results. It should be noted that the reference values, i.e. the initial area  $A_0$  or force  $F_0$  used in the subsequent analyses were determined numerically. Using the empirical laws from formulae (2.9)–(2.15) was found to lead to approximately the same results with relative errors of about 3%. The empirical laws reported by Kogut and Etsion [144] were found to lead to approximately the same results with error levels in the range of 3–5% except for cases with very small or very high yield stress  $\sigma_Y$ . In those cases, Jackson and Green's results reproduced the simulations more faithfully.

For future use, the normalized interference  $\delta^*$  is defined by

$$\delta^* = \frac{\delta}{\delta_c}, \quad (2.16)$$

the normalized asperity contact area  $A^*$  by

$$A^* = \frac{A}{A_c} \quad (2.17)$$

and the normalized asperity force  $F^*$  by

$$F^* = \frac{F}{F_c}. \quad (2.18)$$

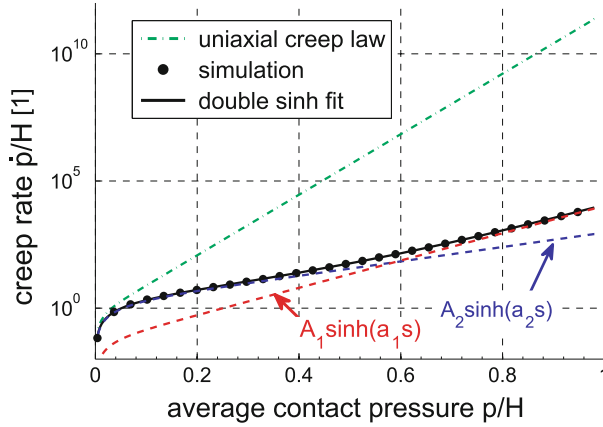


Fig. 2.3 Creep law  $\dot{p}(p) = \partial p / \partial \tau$  for parameter set 1, Table 2.1

### 2.2.2 Creep Process

In Fig. 2.2, the force  $F$  and contact area  $A$  in dependence on normalized creep time

$$\tau = t / (H / C_1 E) \quad (2.19)$$

(see Sect. 2.2.4 for details) is shown for a reference parameter set. The parameters, given as set number 1 in Table 2.1 on page 19, are typical for an iron- or steel-type material and an asperity in the fully plastic contact regime. Because the transition to fully plastic behavior occurs at an interference of about  $\delta_t \approx 70\delta_c - 80\delta_c$  [128, 144], an interference of  $\delta = 100\delta_c$  was chosen to be safely within the fully plastic region. The contact force shows a characteristic creep behavior with a steep initial decline and an increasingly slower creep in later stages. The area, on the other hand, stays nearly constant after a fast initial creep-induced enlargement of about 7 %. In this section, a qualitative interpretation of the evolution is presented which will be extended by quantitative empirical laws in Sects. 2.2.3 and 2.2.4.

To analyze the stress relaxation in more detail, the time derivative of the average pressure  $p = F/A$  is shown in Fig. 2.3 for the simulation of parameter set 1 in Table 2.1 on page 19. (Note that the derivative  $\dot{p}$  is in terms of the dimensionless time of equation (2.19), i.e.  $\dot{p} = \partial p / \partial \tau$ , and therefore dimensionless.) Superficial inspection exposes the overall hyperbolic sine law, reflecting an exponentially larger creep rate  $\dot{\epsilon}_{cr}$  for higher stress  $\sigma$  or pressure  $p$  and a linear relation for small stress (note that in the logarithmic plot of Fig. 2.3, exponential increase corresponds to a straight line). Close inspection reveals, however, that two slopes in the  $\dot{p}$  curve can be identified. While the fit curves will be explained in more detail in Sect. 2.2.4, it can clearly be seen that the stress release is significantly faster for contact pressures

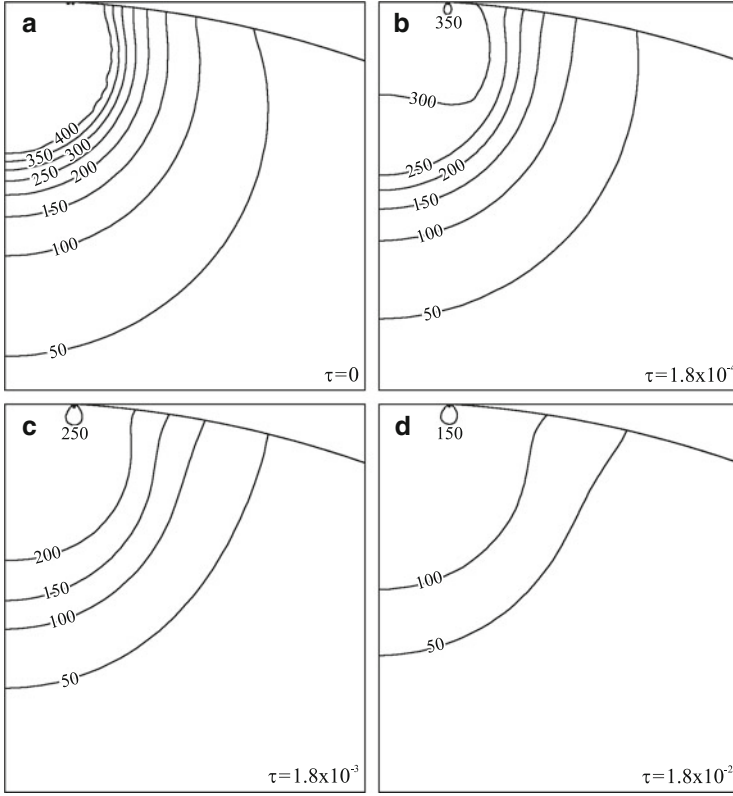


**Fig. 2.4** Distribution of equivalent stress  $\sigma$  for different stages of the creep process. The stress line values are given in MPa

$p \geq 0.6H$ , resulting in a steeper slope. This fact cannot be explained merely by the area increase visible in Fig. 2.2, as was carefully tested.

The explanation for this interesting creep behavior lies in the special contact geometry of the spherical asperity. As shown in prior analyses [144], the stresses in a deformed half-sphere are concentrated near the contact area. This is also visible in Fig. 2.4a, where the von Mises stress distribution at the beginning of the creep process is shown. Initially, a spherical region below the contact zone is at full yield stress and therefore has a high creep ratio. Not shown in the graphs is the average surface pressure  $p$  which, along with the von Mises stress in this region, is also significantly elevated up to the hardness  $H$ . This is significantly higher than the yield stress, although the exact value of the hardness of course depends on several parameters and is not a unique property of the material [128] (The hardness  $H$  for Fig. 2.3 was derived numerically from the simulations, not from the equations presented in [128], although the differences were found to be small).

The central contact region of an asperity with its high pressure is contained and stabilized by the surrounding asperity material unloaded by the contact. However,

this containment relaxes during creep and can no longer contain the high-pressure region. Therefore, the material in the center of the asperity expands, which causes an increase in the contact area as seen in Fig. 2.2. This effect is augmented by the normal creep expansion visible also for cylindrical contacts (see Sect. 2.2.3). When expanding, the center material pushes aside the surrounding material and induces new shear stresses. This can be clearly seen in Fig. 2.4b, c where a small elliptical region near the very edge of the contact line shows significantly increased von Mises stress. As soon as the pressure is released at a contact pressure of about  $p \approx 0.6H$  in Fig. 2.3, the area increase stops. This coincides with the transition of the  $\dot{p}$  curve to a shallower slope. This additional relaxation mechanism can therefore be plausibly held responsible for the accelerated creep rate during the first creep phase. This is also the main difference with regard to the case of a cylinder contact under creep. Assuming frictionless face surfaces in line with the present study, a uniaxial stress state is present throughout the volume. Therefore, a containment effect is absent.

## 2.2.3 Contact Area

### 2.2.3.1 Mode of Contact Area Evolution

In this section, quantitative results about the behavior of the contact area are presented. It should be stressed that the growth of the initial contact area  $A_0$  is a relatively minor effect, only increasing the area by some 10 %. Additionally, the detection of the contact area in the simulation is affected by relatively large errors due to the finite number of nodes in the contact interface: In accordance with previous simulations [128, 149], the contact radius is detected when a node establishes or loses contact, therefore introducing granularity. In between the measured data, the curve is interpolated. Even with the very fine boundary mesh described in Sect. 2.1, a relative error in the contact area of about 0.7 %  $A_0$  is to be expected, which translates to a substantial error in the relative area change.

In Fig. 2.5, the area increase of Fig. 2.2 is displayed enlarged and with error bars. The errors were calculated based on the assumption that both the individual contact areas  $A(t)$  and  $A_0$  have about 0.7 % relative error. The errors therefore include the possibility of a large systematic error. It can be seen that after an initial fast rise, the relative area change plateaus.

This behavior is similar to the behavior of a simple cylinder under creep relaxation. By comparison with the cylindrical case, an approximate functional dependency of the area evolution can be derived. In a cylinder oriented and compressed along the z-axis, a uniaxial stress tensor is assumed which is associated with the following strain tensor, split according to (2.1),

$$\boldsymbol{\varepsilon} = \boldsymbol{\varepsilon}_{el} + \boldsymbol{\varepsilon}_{cr} = \begin{pmatrix} -\nu \varepsilon_{el} & & \\ & -\nu \varepsilon_{el} & \\ & & \varepsilon_{el} \end{pmatrix} + \begin{pmatrix} -\nu_{pt} \varepsilon_{cr} & & \\ & -\nu_{pt} \varepsilon_{cr} & \\ & & \varepsilon_{cr} \end{pmatrix}. \quad (2.20)$$

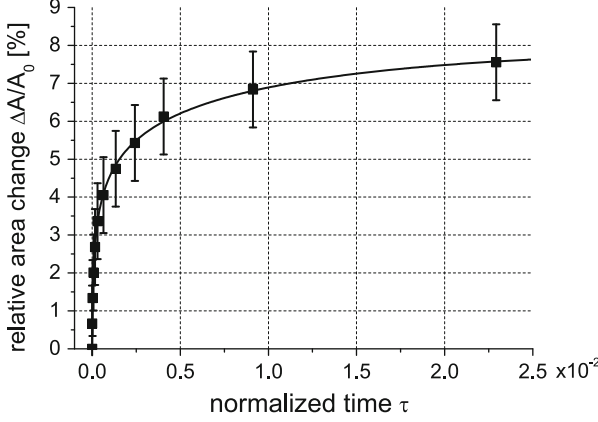


Fig. 2.5 Normalized area change, enlarged from Fig. 2.2

Note that the creep strain is similar to the plastic strain in that it is conserving the volume [13]. Therefore, all occurrences of the creep strain  $\varepsilon_{cr}$  are associated with a Poisson ratio of  $\nu_{pl} = 1/2$ , while the elastic strain  $\varepsilon_{el}$  causes a volume reduction and is therefore associated with the Poisson ratio  $\nu < 1/2$  from Table 2.1 on page 19. A fixed boundary condition in the z-direction imposes the constraint  $\varepsilon_0 = \varepsilon_{el} + \varepsilon_{cr}$ , where  $\varepsilon_0$  is the (constant) initial elastic strain at the start of the creep process. The creep law (2.7) for the uniaxial case and  $\sigma = E\varepsilon_{el}$  yields the ODE (ordinary differential equation)

$$\dot{\sigma} = E\dot{\varepsilon}_{el} = -E\dot{\varepsilon}_{cr} = -EC_1 \sinh(C_2\sigma) \quad (2.21)$$

which has the solution  $\sigma = \frac{2}{C_2} \operatorname{artanh}(\exp(-C_1C_2Et + \xi))$ , where  $\xi$  is an integration constant to be determined from the initial condition. The contact radius in the x-direction can be calculated as  $r(t) = r(0)(1 - \varepsilon_{cr}/2) = r(0)(1 - (\varepsilon_0 - \varepsilon_{el})/2)$  which yields a contact area of

$$A(t) = \pi r(t)^2 \approx A_0 \left[ 1 - (1 - 2\nu) \left( \varepsilon_0 - \frac{2}{EC_2} \operatorname{artanh}(-C_1C_2Et + \xi) \right) \right], \quad (2.22)$$

where quadratic terms in  $1/EC_2$  were omitted.

Therefore, for the further analysis, a time evolution law according to the equation

$$\frac{\Delta A(t, C_2, \delta)}{A_0} = \frac{\Delta A(C_2, \delta)}{A_0} [1 - 2c(\gamma_1, \gamma_2) \operatorname{artanh}\{\exp(-\gamma_1\tau(t) + \gamma_2)\}], \quad (2.23)$$

was fitted to the data where  $c(\gamma_1, \gamma_2)$  was chosen such that  $\Delta A(t = 0) = 0$  or

$$c(\gamma_1, \gamma_2) = [2 \operatorname{artanh}(\exp(\gamma_2))]^{-1}. \quad (2.24)$$

For the definition of  $\tau(t)$  see Eq. (2.33). The resulting fit is shown in Fig. 2.5 for the reference parameter set (set number 1 in Table 2.1 on page 19). The fit parameters  $\gamma_1$  and  $\gamma_2$  were found to be

$$\gamma_1 = 27 \pm 5 \quad \text{and} \quad \gamma_2 = -(1 \pm 0.4) \cdot 10^{-3}. \quad (2.25)$$

The error margins were calculated at 66 % confidence bounds by the nonlinear fitting algorithm. For the amplitude  $\Delta A(C_2, \delta)$  see Sect. 2.2.3.2. The corresponding fit is shown in Fig. 2.5 and proves that Eq. (2.23) captures the trend of the data well. This result indicates that the first creep relaxation phase of an asperity is indeed dominated by a pressure release mechanism. Although the details of the stress evolution are significantly different as described in Sect. 2.2.2 and shown in Fig. 2.4, the effective parameters given in Eq. (2.25) are apparently sufficient to capture the physics of the problem.

### 2.2.3.2 Parameter Study on Contact Area Evolution

It is now interesting to analyze which input parameters have a significant influence on the area increase. For this purpose, extensive parameter studies as indicated in Table 2.1 on page 19 were performed. The variation of the radius  $R$  and interference  $\delta$  was aimed at the basic geometry of the problem. These parameters are especially important in the context of a friction model where a statistical ensemble of asperities with different heights and radii is usually examined. The influence of the material parameters Poisson's ratio  $\nu$ , yield stress  $\sigma_Y$  and Young's modulus  $E$  as well as the material creep law parameters  $C_1$  and  $C_2$  were analyzed to obtain a certain degree of universality of the presented empirical laws for different kinds of metals. It should be noted, however, that the presented laws can only be valid in proximity to the reference parameters indicated in set number 1 in Table 2.1 on page 19. Further, the parameter  $C_1$  simply determines the characteristic time scale of the creep and was chosen to ensure numerical convergence. Variations of this parameter were simply performed to test for numerical errors in the time integration.

The parameters in Eq. (2.25) are associated with rather large error bounds. Additionally, the relatively high systematic errors, indicated by the error bars in Fig. 2.2, further increase the uncertainty. It is therefore hard to estimate if the parameters  $\nu$ ,  $E$ ,  $R$  and  $\sigma_Y$  have a systematic influence on the area evolution. While a certain variation is visible, model (2.23) with parameters (2.25) fits all experiments as indicated in sets 2, 4, 5 and 6 in Table 2.1 on page 19 within the respective error bars. Further research with improved accuracy is needed. To produce reliable results, the study therefore focused on the parameters  $C_2$  and  $\delta$  which show a significant influence on the area evolution.

The interference  $\delta$  determines the initial contact area  $A_0(\delta)$  as described by Jackson and Green's empirical formula (2.9). The maximum area increase due to creep is shown in Fig. 2.6 for the simulation set 3 in Table 2.1 on page 19, i.e. for variation of interference  $\delta$  and therefore initial area  $A_0$ . It can be established that the

**Fig. 2.6** Maximum area change  $\Delta A$  for variation of the initial area  $A_0$

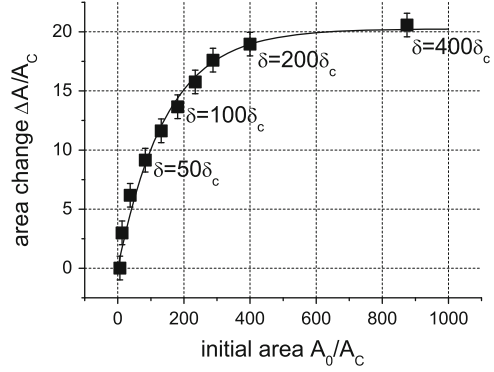
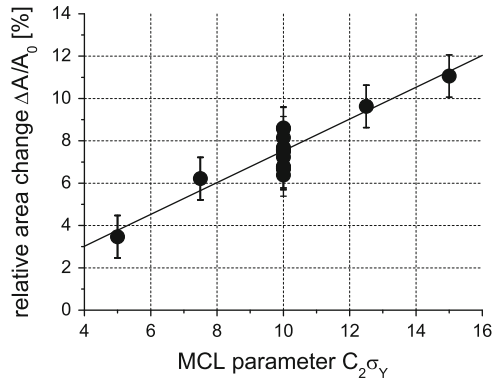


**Fig. 2.7** Maximum area change  $\Delta A$  for variation of the creep parameter  $C_2$



area increase  $\Delta A$  levels off at an interference of about  $200\delta_c$ . The form of the data suggests a fit by an exponential curve and was found as

$$\Delta A(\delta)|_{C_2=10/\sigma_Y} = (20.2 \pm 0.7)A_c \left[ 1 - \exp \left( -\frac{A_0(\delta)}{(146 \pm 14)A_c} \right) \right]. \quad (2.26)$$

The errors are statistical errors (66 % confidence interval) calculated by the nonlinear fitting algorithm.

The parameter  $C_2$  determines how sensitive the creep rate is to the absolute stress value, i.e. how much faster the material creeps due to higher local stress. Because the highest stress levels are reached in proximity to the contact area, it is plausible that  $C_2$  and the magnitude of area increase,  $\Delta A$ , are positively correlated. In Fig. 2.7, the relative area increase  $\Delta A/A_0$ , normalized against the initial area  $A_0$ , is shown in dependence on  $C_2$ . The simulations were performed for constant  $\delta$  according to the parameters in set number 7 in Table 2.1 on page 19. This parameter dependence follows a simple linear relationship

$$\frac{\Delta A(C_2, \delta)}{A_0} = \frac{\Delta A(\delta)|_{C_2=10/\sigma_Y}}{A_0} + (0.75 \pm 0.12) \frac{C_2}{\sigma_Y}, \quad (2.27)$$

where the intercept at  $C_2 = 10/\sigma_Y$  is given by Eq. (2.26) in dependence on the interference  $\delta$ . A cross-correlation between the interference  $\delta$  and  $C_2$  is not expected and was not seen in the limited simulations conducted on this issue.

Concluding the parameter study of the area evolution, Eqs. (2.23) with (2.25), (2.26) and (2.27) now give a full empirical description of the area evolution during creep, including the dependence on the most important parameters.

### 2.2.4 Contact Force and Pressure

In the following paragraphs, quantitative empirical laws will be offered for the important evolution of the average contact pressure  $p(t)$  and accordingly, the relaxation rate  $\dot{p}$ . To simplify the discussion, this functional relationship will henceforth be called the *geometrical creep law* (GCL) to distinguish it from the *material creep law* (MCL) given in Eq. (2.7). For a cylindrical geometry under constant strain, i.e. the case of uniaxial stress and creep, both laws show an identical structure. Using  $p = \sigma$ , for this case, it follows that  $\dot{p} = -EC_1 \sinh(C_2 p)$ . For comparison with the simulated relaxation law for the spherical geometry, this law is plotted in Fig. 2.3 as a dash-dotted line. It is obvious that the creep relaxation for a cylindrical geometry is more efficient because a cylinder has a homogeneous stress state, while large portions of the sphere in contact are initially at a low equivalent stress and therefore creep much more slowly.

As presented in Sect. 2.2.2, the GCL for the spherical geometry shows a change in slope around  $p = 0.6H$ . As an analytical approximation of this behavior, we propose a double hyperbolic sine law

$$\dot{p}(p) = \sum_{i=1}^2 A_i \sinh(\alpha_i p) \quad (2.28)$$

which is shown in Fig. 2.3 as a solid curve. The fit components for  $i = 1, 2$ , respectively, are plotted as dashed curves for comparison. These components can be interpreted as the low stress and high stress behavior, both following their own hyperbolic sine creep law. For the reference parameter set of Fig. 2.3, the constants are  $A_1 = (2.99 \pm 0.04)EC_1$ ,  $\alpha_1 = (6.10 \pm 0.08)/\sigma_Y$  and  $A_2 = (0.17 \pm 0.01)EC_1$ ,  $\alpha_2 = (12.09 \pm 0.06)/\sigma_Y$ . The components show the same structure as the MCL. As such, creep law (2.28) is physically plausible, i.e. it follows an exponential law for high stress and satisfies the boundary condition  $\dot{p}(p = 0) = 0$ . Generally, the fit parameters  $A_i$  and  $\alpha_i$  are dependent on the input parameters. In the following paragraphs, a detailed parameter study similar to Sect. 2.2.3.2 will be presented.

#### 2.2.4.1 Geometric Parameters Radius $R$ and Interference $\delta$

The variation of the asperity radius  $R$  within the bounds given in set number 2 in Table 2.1 on page 19 showed no significant change in the creep law. The resulting

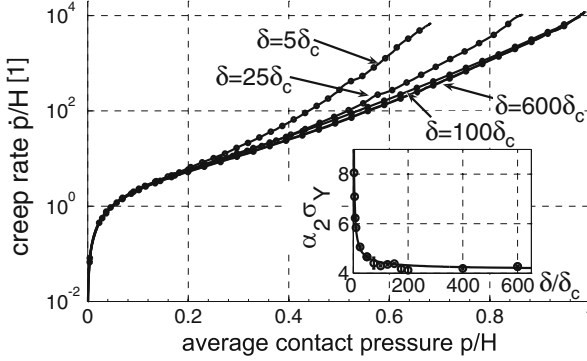


**Fig. 2.8** Creep law  $\dot{p}(p) = \partial p / \partial \tau$  for variation of the interference  $\delta$ . *Inset:* Fit parameter  $\alpha_2$

creep rates deviated by less than 3 %, which is on the order of the numerical errors. It should be noted that as the compression stage was always performed up to an interference of  $100\delta_c$  and  $\delta_c \propto R$  as given in Eq. (2.10), this universality is a direct consequence of the normalization to critical interference.

On the other hand, the variation of the interference  $\delta$  cannot be expected to show this simple universal behavior. In Fig. 2.8, the geometrical creep laws for a variety of interferences  $\delta$  as given in set number 3 in Table 2.1 on page 19 are shown. It was generally found that the GCL showed little variation for a wide range of interferences  $\delta$ . For the range  $50\delta_c \leq \delta \leq 400\delta_c$ , the average deviation was below 5 % and therefore within the numerical errors. The creep law for  $\delta = 25\delta_c$  however deviated by 25 % from the creep law for the reference interference  $\delta = 100\delta_c$ . This result illustrates that the presented GCL and its parameters are only valid for fully plastic asperities. The lower bound of validity should conservatively be estimated at the transition interference to fully plastic asperity behavior at  $\delta_t \approx 70\delta_c - 80\delta_c$  [128, 144]. Elastic or elasto-plastic asperities show a different creep behavior as further illustrated by the widely deviating creep law for an interference of  $\delta = 5\delta_c$  in Fig. 2.8. Inspection of the stress evolution indicates that the mechanisms of asperity creep are different in this region. Further results will be presented in the generalized asperity model in Sect. 4.4.

The creep law for larger interferences  $\delta > 100\delta_c$  could be seen to show little variation. Increasing the interference from  $100\delta_c$  to  $600\delta_c$  in Fig. 2.8 only changed the creep law by about 9 %. Because a change of the FEA mesh was necessary to accomplish the simulation of such large interferences, this error still lies within the numerical scatter of the simulations. It was therefore not possible to establish a deviation from universality for large interferences up to  $600\delta_c$ . This fact is further illustrated by the plot of the fit parameter  $\alpha_2$  in the inset of Fig. 2.8. While a rapid variation up to interferences of  $100\delta_c$  is visible, the parameter stays virtually constant above that. Of course, for a very much larger interference, i.e. a completely flattened asperity (see Jackson and Green [128]), this behavior must be expected to break down eventually.

### 2.2.4.2 Material Parameters Young's Modulus, Yield Stress and Poisson's Ratio

The dependence of the GCL on the Poisson ratio  $\nu$  was analyzed by a set of numerical simulation experiments where the Poisson ratio was varied between  $\nu = 0.28$  and  $\nu = 0.38$  (set number 4 in Table 2.1 on page 19, about 30 simulations of 5 different values of  $\nu$ ) which covers most engineering metals. It was found that the Poisson ratio has only a negligible influence on the GCL of about 3 %, which is well within the numerical errors of the simulations. Its influence will therefore be ignored in further discussion.

On the other hand, the influence of Young's modulus  $E$  and yield stress  $\sigma_Y$  was found to be profound (in about 100 simulations of 5 different values of  $E$  and 5 different values of  $\sigma_Y$ ). The influence of these material parameters can be understood from the uniaxial creep law (2.7). In Sect. 2.4, it is shown how different boundary conditions in the full tensorial treatment only lead to a small change in the prefactor. For the simple uniaxial case, the creep equation

$$\dot{\varepsilon}_{cr} = C_1 \sinh(C_2 \sigma), \quad (2.29)$$

is considered where  $\dot{\varepsilon}_{cr}$  is the creep component of the total strain  $\varepsilon_{tot} = \varepsilon_{cr} + \varepsilon_{pl} + \varepsilon_{el}$ . Assuming for the moment that the total and plastic strain are constant such that  $\dot{\varepsilon}_{el} = -\dot{\varepsilon}_{cr}$ , it follows that

$$\dot{\sigma}(\sigma) = -E \dot{\varepsilon}_{cr} = -E C_1 \sinh(C_2 \sigma). \quad (2.30)$$

Comparing asperities of a metal 1, say, with a yield stress  $\sigma_Y$  with those of an alternative metal 2 with a different yield stress  $\tilde{\sigma}_Y = \beta \sigma_Y$  (i.e. both metals differ by a factor of  $\beta$  in their yield stress), the creep rates can be called equal if

$$\dot{\sigma}(\gamma \tilde{\sigma}_Y) = \dot{\sigma}(\gamma \sigma_Y) \quad (2.31)$$

at arbitrary  $\gamma$ . This value  $\gamma$  here signifies the stress scaled to respective yield stress value.

Equation (2.31) holds if either  $\tilde{E} = \beta E$  or  $\tilde{C}_1 = \beta C_1$  as well as  $\tilde{C}_2 = C_2/\beta$ . To find a universal scaling law, the normalized stress  $z' = \sigma/\sigma_Y$  is introduced (the prime ' indicates the uniaxial case), and it follows

$$\dot{z}' = - \underbrace{\frac{E C_1}{\sigma_Y}}_{1/t'_1} \sinh(C_2 \sigma_Y z'), \quad (2.32)$$

where  $t'_1$  is therefore the characteristic time of creep for the uniaxial stress case.

From this qualitative derivation one can see that for the uniaxial case (a) when considering normalized stress, the creep law is stationary for  $E C_1/\sigma_Y$  and  $C_2 \sigma_Y$  constant, (b) a change in  $E$  or  $C_1$  is equivalent to a change of the characteristic time

scale (see Sect. 2.2.4.3) and (c) a scaling of  $\sigma_Y$  has the same effect as a reciprocal scaling of  $C_2$  by the same ratio (see Sect. 2.2.4.3) and a proportional scaling of  $E$  or  $C_1$ . With this argumentation, the number of independent parameters can be reduced from  $E, C_1, C_2, \sigma_Y$  to, for example,  $t'_1$  and  $C_2$ .<sup>2</sup>

For a spherical geometry, the argumentation above still holds approximately but is complicated by two additional effects. For one, the hardness of the asperity is dependent on the contact radius as found recently by Jackson and Green [128] (see Eq. (2.13)). While the correct scaling for the MCL is therefore  $z' = \sigma/\sigma_Y$ , for the GCL it was found that  $z = p/H$  leads to better universality. The characteristic time is therefore  $t_1 = H/EC_1$ . As an illustration of this behavior, the  $p(t)$  curves of simulation run 5 as in Table 2.1 on page 19 were scaled by both approaches and compared the average deviation of the curves. For scaling by  $\sigma_Y$  and  $t'_1$ , deviations of up to 25 % were found while the scaling law for scaling by  $H$  and  $t_1$  only showed a maximum error of 3 %. For all figures in this chapter a normalized time

$$\tau = t/t_1 = t \frac{EC_1}{H}. \quad (2.33)$$

was therefore used. The hardness  $H$  was calculated from Eq. (2.13), which corresponds closely to the simulation results.

The second effect complicating the scaling argumentation relates to the above assumption of a purely uniaxial stress state. As has already been discussed, the stress distribution in Fig. 2.4 is rather complex and an involved expansion process with the buildup of shear stress at the rim of the contact region takes place. Actually, creep only *directly* relaxes the deviatoric parts of the stress tensor (see Sect. 2.4) and therefore the shear energy  $dU_d/dV = \frac{1}{2}s_{ij}e_{ij}$  where  $s$  denotes the stress deviator tensor as defined on page 20 in association with Eq. (2.4), and  $e$  denotes the strain deviator tensor. In the reference case (see set number 1 in Table 2.1 on page 19), the shear energy initially contains about 70 % of the total elastic energy  $dU_t/dV = \frac{1}{2}\sigma_{ij}\epsilon_{ij}$ . The rest of the energy, i.e. the pressure components and the corresponding energy  $dU_p/dV = dU_t/dV - dU_d/dV = \frac{1}{2}pe_{kk}$ , are partially dissipated by damping when the material expands and partially transformed into shear energy which is then again relaxed by creep. The simple scaling law (2.33) can no longer be proven to hold exactly. However, the dependence on the boundary conditions is exemplarily shown in Sect. 2.4 to lead to a change in the prefactor only. It does *not* change the fundamental dependency of the characteristic time  $t_1$

<sup>2</sup>According to the Buckingham  $\Pi$  Theorem [50], even a further reduction to just one parameter is possible. To see this, consider the definition of dimensionless time by  $\tau' = EC_1/\sigma_Y$ , and dimensionless stress argument  $\mathcal{E} = C_2\sigma_Y z'$ . Then Eq. (2.32) reduces to  $\partial\mathcal{E}/\partial\tau = -\gamma \sinh(\mathcal{E})$  with just one dimensionless parameter  $\gamma = \sigma_Y C_2$ . However, as will be explained in the paragraph leading to Eq. (2.33), the spherical geometry has a complicated initial condition (i.e. stress distribution at time  $t = 0$  s). Characterizing this initial stress distribution adds parameters in terms of the Buckingham  $\Pi$  theorem, such that the reduction to just one dimensionless parameter breaks down in this generalized case. It was therefore not analyzed any further.

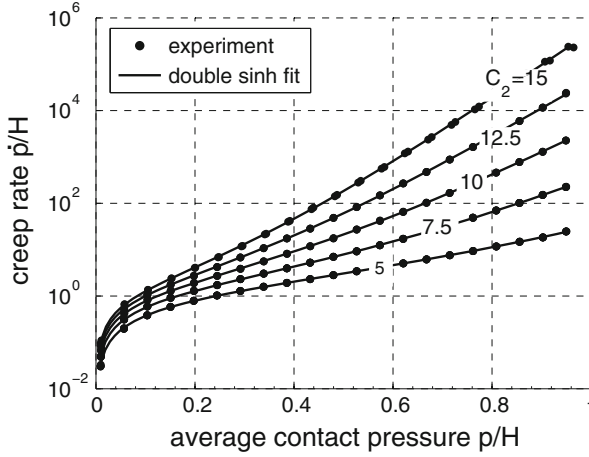


Fig. 2.9 Creep law  $\dot{p}(p)$  for variation of the creep parameters  $C_1$  and  $C_2$

on the material parameters. This result was validated by varying Young's modulus  $E$  and yield stress  $\sigma_Y$  according to set numbers 5 and 6 in Table 2.1 on page 19 and plotting the creep rate in a plot like Fig. 2.3. It is easily seen that a scaling according to Eq. (2.33) would lead to coincident curves. The average deviation between the curves was under 5 % which is on the order of the numerical errors. It is therefore concluded that even in the complex case of a spherical geometry, the simple scaling law (2.33) approximately holds as long as a normalization to the hardness  $H$  (e.g. from Eq. (2.13)) is used in place of the yield stress  $\sigma_Y$ .

### 2.2.4.3 Creep Parameters $C_1$ and $C_2$

The creep parameter  $C_1$  has already been found in Sect. 2.2.4.2 to determine the characteristic time scale according to Eq. (2.33). Compensating for the influence of  $C_1$  by normalizing the time scaling according to (2.33), the influence of the creep parameter  $C_2$  is analyzed for a range of creep parameters, given as set number 7 in Table 2.1 on page 19. The results are shown in Fig. 2.9. It was found that for higher values of  $C_2$ , the creep rate for high contact pressures increases significantly. This behavior reflects the role of  $C_2$  in the material creep law (2.7), where the creep rate depends exponentially on the term  $C_2\sigma$ . In addition, the characteristic change of slope in the creep rate law described in Sect. 2.2.2 is most pronounced for values of  $C_2 \approx 10/\sigma_Y$ . For much lower values, the acceleration of the creep process in the first phase is weak, which is also witnessed by the small area increase for low  $C_2$  (see Sect. 2.2.3.2 and Fig. 2.7). For higher values of  $C_2$ , the high-stress creep process of the first phase overshadows the low-stress behavior of the second phase.

The curves are each well approximated for themselves by a double hyperbolic sine fit in the form (2.28) with an error of less than 4 %. The fit yields four fit

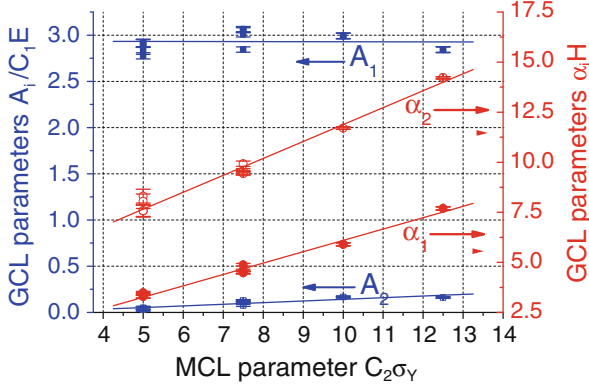


**Fig. 2.10** Fit parameters  $A_i$  (left axis),  $\alpha_i$  (right axis) for variation of the creep parameters  $C_1$  and  $C_2$

parameters  $A_1, A_2, \alpha_1, \alpha_2$  for each curve. Analyzing these parameters' dependence on the material creep constant  $C_2$  uncovers a remarkably simple relation. As shown in Fig. 2.10 for parameter set 7 in Table 2.1 on page 19, the fit parameters fall approximately on a straight line when plotted against the MCL input parameter  $C_2$ . The parameter  $C_1$  has no systematic influence.

A unified geometric creep law in the following form is therefore proposed:

$$\dot{p} = A_1 \sinh(\alpha_1 p) + A_2 \sinh(\alpha_2 p) \quad (2.34)$$

$$\begin{pmatrix} A_1 \\ A_2 \end{pmatrix} = EC_1 \left\{ \begin{pmatrix} 2.933 \pm 0.076 \\ -0.035 \pm 0.019 \end{pmatrix} + C_2 \sigma_Y \begin{pmatrix} 0.001 \pm 0.010 \\ 0.018 \pm 0.002 \end{pmatrix} \right\} \quad (2.35)$$

$$\begin{pmatrix} \alpha_1 \\ \alpha_2 \end{pmatrix} = \frac{1}{H} \left\{ \begin{pmatrix} 0.43 \pm 0.14 \\ 3.43 \pm 0.23 \end{pmatrix} + C_2 \sigma_Y \begin{pmatrix} 0.57 \pm 0.02 \\ 0.85 \pm 0.03 \end{pmatrix} \right\} \quad (2.36)$$

which has eight fit parameters and fits all creep rate simulations performed within an error of about 6%. The error bars shown in Fig. 2.10 are error bounds at a 66% confidence level from the nonlinear curve fitting algorithm. The scatter of the data points stems from the choice of different values for  $C_1$  and therefore gives an impression of the numerical scatter of the time integration algorithm and its effect on the fitting parameters. Both types of error give the same qualitative picture for the accuracy of the data points. Error levels in Eqs. (2.34)–(2.36) are 66% confidence level error bounds from the linear curve fitting algorithm.

## 2.3 Discussion

In this chapter, the creep relaxation modes of an asperity in fully plastic contact were demonstrated, assuming a hyperbolic sine creep law. The creep process was found to consist of two phases. The first phase consisted of a fast relaxation with a

simultaneous area increase. In the second phase, the contact area was constant and the relaxation process was slowing considerably. The detailed analysis of the stress evolution inside the asperity shows for the first stage a stress buildup close to the very edge of the contact region, contrary to the expected stress reduction. In the second phase, the asperity as a whole loses its stress.

For the stress relaxation, this behavior can be well approximated by the sum of two hyperbolic sine creep laws, with one summand describing the high stress behavior and one describing the low stress behavior. The area evolution can be surprisingly well described by the simple formula for the area increase of a cylinder under creep. This is the case in spite of the evolution of the stress distribution in the asperity showing a behavior that is significantly different from that of a cylinder. It is therefore possible to conclude that the assumption of a cylindrical contact geometry for an asperity junction under creep by Brechet and Estrin [43] or Persson [191] is justified in hindsight.

Furthermore, detailed empirical formulae have been given to quantitatively describe the creep behavior of an asperity. The double hyperbolic sine law for the stress relaxation is valid down to an interference of about  $\delta = 50\delta_c$ . The law shows a surprising generality towards the input material and geometrical parameters. Only the dependence on the parameter  $C_2$  had to be fitted numerically and even here a simple linear relation was found. The area evolution showed a slightly more complex behavior, depending both on the interference  $\delta$  and the creep parameter  $C_2$ . Empirical laws for the dependence on these parameters were given in Eqs. (2.23), (2.26) and (2.27).

It should be noted that the inclusion of a time or temperature dependent material creep law is straightforward, as long as the hyperbolic sine dependence on stress is retained. In this case, the constant  $C_1$  becomes a time and temperature dependent function  $C_1(t, T)$  and can be included trivially in the ODEs describing the asperity behavior.

At maximum surface pressure, a maximum creep stress reduction of  $\dot{p}(H) \approx 10^4 H$  can be determined from Fig. 2.3 for the reference parameter set. Calculating  $1/t_1 \approx 10^{-3} - 10^{-4} \text{ s}^{-1}$  with  $C_1 \approx 10^{-3} \text{ s}^{-1}$  for an iron-type material as stated above, a maximum stress derivative of  $dp/dt = H \text{ s}^{-1}$  and therefore significant relaxation and area increase on a time scale of 1 s can be expected. If we further assume a typical asperity of diameter  $D = 100 \mu\text{m}$ , an interaction time of 1 s would be achieved for a speed of roughly  $v = 10^{-4} \text{ m/s}$  which compares favorably with the literature [206]. Although a more thorough analysis of creep effects in sliding friction will be presented in Chap. 3, this rough analysis confirms the findings of previous studies [43] in that creep effects could indeed be held responsible for the velocity-dependent dry friction of certain metallic materials.

## 2.4 Addendum: Tensorial Creep Law

Equation (2.30) describes the creep evolution of a uniaxial stress state. In the full 3D case, the evolution depends on the boundary condition. For comparison, the evolution of a uniaxial stress state with fixed boundary condition  $\dot{\epsilon}_{tot} = 0$  on *all*

borders is considered here. This is in contrast to the uniaxial case considered for Eq. (2.30), where only the strain in the principal stress direction  $\dot{\epsilon} = \dot{\epsilon}_{tot,z} = 0$  is fixed. This model case sheds some light on the creep relaxation inside the contained, high pressure center of the asperity. Because of the symmetry and the homogeneity of the material, the total strain is constant throughout the bulk of the material which means that  $\dot{\epsilon}_{el} = -\dot{\epsilon}_{cr}$ .

An arbitrary stress state  $\sigma$  can be split into a pressure part  $\mathbf{p} = \frac{1}{3}\text{tr}(\sigma)\mathbf{I}$  with  $\mathbf{I}$  the identity tensor and a traceless, deviatoric part  $\mathbf{s} = \sigma - \mathbf{p}$ . Thus, the tensorial creep law (2.4) for the simple case of small strain and isotropic material law yields a creep direction [89]

$$\begin{aligned} r_{ij} &= \frac{\partial F(\sigma)}{\partial \sigma_{ij}} = \frac{\partial}{\partial \sigma_{ij}} \sqrt{\frac{3}{2} s_{kl} s_{kl}} \\ &= \frac{3}{\sigma} s_{kl} \left( \frac{\partial}{\partial \sigma_{ij}} \left( \sigma_{kl} - \frac{1}{3} \delta_{kl} \sigma_{mm} \right) \right) = \frac{3}{\sigma} s_{ij}. \end{aligned} \quad (2.37)$$

Starting from Eq. (2.4), using the identity  $\mathbf{s} : \sigma = \mathbf{s} : (\mathbf{s} + \mathbf{p}) = \mathbf{s} : \mathbf{s}$  it is found that

$$\dot{\epsilon}_{cr} : \sigma = \frac{1}{f} \dot{\epsilon}_{cr}(\sigma) \frac{3}{2} \mathbf{s} : \sigma = \frac{1}{f} \dot{\epsilon}_{cr}(\sigma) \sigma^2 \stackrel{!}{=} \dot{\epsilon}_{cr}(\sigma) \sigma, \quad (2.38)$$

where the last relation is gained from imposing energetic equivalence of the tensorial law with the uniaxial law. (Note that  $\dot{\epsilon}_{cr}$  denotes the full creep tensor, while  $\epsilon_{cr}(\sigma)$  denotes the uniaxial, scalar creep law as in Eq. (2.4).) Therefore, the normalization factor  $f = 1/\sigma$  is found. Together with  $\mathbf{s} = \mathbf{C} : \mathbf{e} = 2G\mathbf{e}$  where  $\mathbf{e}$  denotes the deviatoric component of the strain tensor  $\epsilon$ ,  $\mathbf{C}$  the elasticity tensor and  $G$  the shear modulus, it is now possible to formulate the full 3D creep law (2.4) in the simplified form

$$\dot{\epsilon}_{cr} = \frac{\dot{\epsilon}_{cr}(\sigma)}{\sigma} 3G \mathbf{e} = \frac{\dot{\epsilon}_{cr}(\sigma)}{\epsilon_{eq}} \frac{1}{2(1+\nu)} 3\mathbf{e} \quad (2.39)$$

with the equivalent strain  $\epsilon_{eq} = \sigma/E$ , which is identical to what ANSYS implements for its creep integration (see Sect. 4.3.1.2 in the ANSYS theory manual [9]). With  $\dot{\epsilon}_{el} = -\dot{\epsilon}_{cr}$ , a stress evolution law

$$\dot{\sigma} = -\mathbf{C} : \dot{\epsilon}_{cr} = -\frac{\dot{\epsilon}_{cr}(\sigma)}{\sigma} 3G \mathbf{C} : \mathbf{e} = -\dot{\epsilon}_{cr}(\sigma) 3G \frac{\mathbf{s}}{\sigma} \quad (2.40)$$

follows, i.e. the tensorial creep law for this special case reduces only the deviatoric component of the stress tensor, i.e.  $\sigma(t) = \mathbf{p} + \mathbf{s}(t)$  with a constant pressure tensor  $\mathbf{p}$ .  $\sigma$  creeps towards the pure pressure state  $\mathbf{p}$ . It is known that the time derivative of the equivalent stress is

$$\dot{\sigma} = \frac{\partial}{\partial t} \sqrt{\frac{3}{2} \mathbf{s} : \mathbf{s}} = \frac{3}{2\sigma} \dot{\mathbf{s}} : \mathbf{s}. \quad (2.41)$$

Contracting Eq. (2.40) with  $:\frac{3}{2\sigma}\mathbf{s}$  yields

$$\begin{aligned}\dot{\sigma} &= -\dot{\varepsilon}_{cr}(\sigma)3G\frac{3}{2}\frac{\mathbf{s}:\mathbf{s}}{\sigma^2} = -\frac{3}{2(1+\nu)}E\dot{\varepsilon}_{cr}(\sigma) \\ &= -\frac{3}{2(1+\nu)}EC_1\sinh(C_2\sigma).\end{aligned}\tag{2.42}$$

For this special problem a *faster* creep relaxation by a factor  $c = 3/2(1 + \nu)$  compared to the uniaxial case in Eq. (2.30) is found. The important observation, however, is that the scaling by  $EC_1$  stays intact and therefore so does the normalization of the time scale  $\tau$ .

The factor  $c$  is easy to understand because the pressure tensor  $\mathbf{p}$  is constant in the considered case. The corresponding energy therefore does not undergo relaxation. However, for a typical value of  $\nu = 0.33$ , the additional factor  $c \approx 1.12$  is close to unity, the time scales therefore do not differ significantly from the uniaxial case. Additionally, the assumption of fixed boundaries should be recognized as a severe simplification, as the containing material creeps itself and therefore *releases* the pressure. These are competing effects that elude a simple analytical solution.



<http://www.springer.com/978-3-7091-1505-3>

Transient Effects in Friction

Fractal Asperity Creep

Goedecke, A.

2013, XV, 197 p., Hardcover

ISBN: 978-3-7091-1505-3